

Robust quantum spatial coherence near a classical environment*

Shuyu Zhou, David Groswasser, Mark Keil,* Yonathan Japha, and Ron Folman*

Department of Physics, Ben-Gurion University of the Negev, Be'er Sheva 84105, Israel

(Dated: December 3, 2024)

In quantum physics spatial coherence allows a massive object to be present in two locations at the same time. Such spatial coherence is easily lost in the presence of a classical environment, making it unobservable in our day-to-day experience. Here we report the persistence of spatial coherence for ultra-cold atoms held only $5\ \mu\text{m}$ from a room temperature surface, reducing substantially the distance previously achieved between trapped atoms exhibiting spatial coherence and their classical environment. At this distance, the environment would normally destroy spatial coherence, but we nevertheless observe coherence over a length of $30\ \mu\text{m}$. We show that no observable dephasing is taking place, even on a time scale on the order of one second. From a technological point of view, this may enable quantum devices based on atomic circuits.

A room temperature solid state quantum circuit would have enormous potential and perhaps be as important a development as the long-sought room temperature superconductor. Atom chips [1–3] are a promising candidate but a true analogue of a solid state atomic circuit remains beyond reach, although impressive progress towards clocks, acceleration sensors and quantum information processing on these chips is being made. Alongside this progress towards a technological breakthrough, numerous fundamental experiments have also been made with atom chips (*e.g.*, [4–9]).

To realize a complete “solid state” device with isolated atoms, at least three milestones – adapted from electronic devices – need to be met: arbitrary (*e.g.*, not periodic) guides and traps; single site addressability; and controlled interaction *via* tunneling barriers. The latter requirement demands that potentials must be sculptured with a resolution on the order of the de-Broglie wavelength of the atoms (about $1\ \mu\text{m}$). To achieve these milestones in a scalable device, thereby forming circuits for matter-waves (*e.g.*, [10, 11]), one must be able to trap the atoms and manipulate their external degree of freedom coherently a few micrometers or less from the surface used to generate the potential fields [12]. Interference or diffraction patterns, the hallmark of spatial coherence, have so far been observed for trapped atoms only when held at large distances from the surface [13–18].

We study spatial coherence by loading a Bose-Einstein condensate (BEC) into a lattice potential and observing diffraction. While lattices with trapped atoms close to surfaces have been realized [20, 21] and while diffraction has been observed from atoms dynamically reflected from surfaces [22], we report herein the observation of a diffraction pattern from atoms trapped in a lattice very close to the surface. Specifically, we enter the regime in which the distance of the trapped massive quantum system to a classical environment (and more importantly the correlation length of the noise) is much smaller than the probed coherence length, a regime in which the de-

structive impact of the environment (spatial dephasing) is most effective.

We find that spatial coherence can be maintained for a long time, even very close to the chip surface, and even when the surface is at room temperature, thus creating an extreme temperature gradient. Furthermore, we find that potential corrugations due to material impurities and fabrication imperfections [23–25] may be reduced to a non-inhibiting level. In addition to atomic circuits, this work may enable studies of low dimensional gases with a single sample, ultra-sensitive probing of surface effects such as the Casimir-Polder force and the hypothesized short-range fifth force, as well as devices with matter-waves such as acceleration sensors based on counter-propagating 3D traps moving on a loop (Sagnac) [15, 26]. Finally, a fuller understanding of our experimental results could elucidate the interplay between the rate at which dephasing (*e.g.*, from short-correlation-length Johnson noise) affects the spatial coherence length of a BEC [27, 28] and the rate at which a BEC can phase-lock itself [29].

The experiment is conducted as follows [30]: we create a BEC (typically $10^4\ ^{87}\text{Rb}$ atoms in the $|F = 2, m_F = 2\rangle$ state) and then load a magnetic trap located about $5\ \mu\text{m}$ from the conductive surface of an atom chip, as shown in Fig. 1. The trap potential is modulated to create a magnetic lattice with a $5\ \mu\text{m}$ periodicity along the x direction using only DC currents. The modulation is due to a meandering wire (“snake wire”) which causes the electron current to periodically change direction thus creating magnetic barriers. An additional confining potential is due mostly to a large copper Z-shaped wire (the “trapping wire”) beneath the snake wire, and to fields from external coils [1–3]. Another layer of gold wires on the atom chip is used to fine-tune the position of the cloud along the x direction [31]. As shown in Fig. 1c, the modulation of the potential may be controlled by adjusting the distance of the trap from the surface. Indeed, experiments conducted with an atomic cloud located a few μm further from the surface show no effects due to the potential modulation, while enhanced effects are seen when the cloud is moved closer.

* This manuscript includes in-depth analysis of the data presented in [arXiv:1502.01605](https://arxiv.org/abs/1502.01605).

Corresponding authors: mhkeil@gmail.com, folman@bgu.ac.il

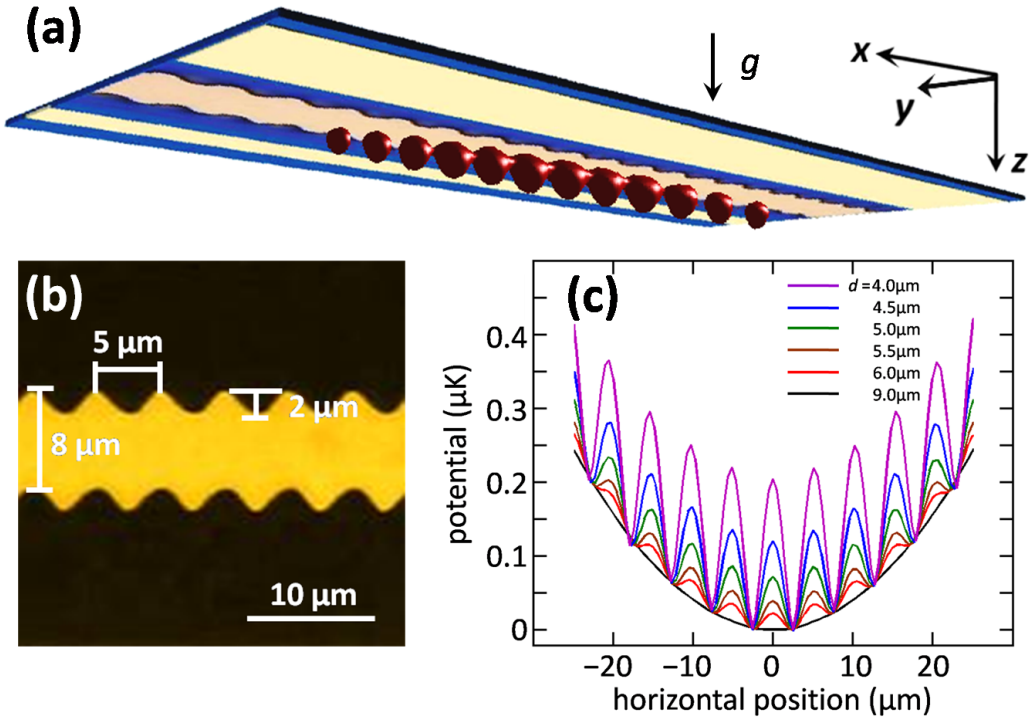


Fig. 1. (Color online) Experimental configuration. (a) An artist's view of the trapped cloud of atoms a few μm from the surface of an atom chip. The atoms are trapped below the surface to allow their state to evolve after release from the trap without falling onto the chip. (b) An optical microscope image of the current-carrying snake wire creating the magnetic lattice potential along the x axis. It adds a magnetic modulation onto the harmonic potential created by the main trapping wire (not shown). The snake wire is made of gold and is 500 nm thick. (c) The modulated potential along the x axis is depicted here together with a weak harmonic potential produced by the trapping wire, giving rise to the atom density profile shown in (a). The trapping wire is used to adjust the distance d of the trap from the snake wire and thereby strongly affects the potential modulation, shown here with the 5 μm periodicity acquired from a snake-wire current of 5.5 mA (adjusting this current fine-tunes the modulation amplitude). Not shown is the radial confinement potential (along the y and z axes) that prevents the atoms from hitting the surface. The imaging beam propagates along the y axis. We do not provide *in situ* images of the modulated atom density because of insufficient imaging resolution.

Aside from the lattice potential, longitudinal confinement *via* a harmonic potential is kept on throughout the trapping. We use a relatively high field of 18.3 G at the trap minimum, thereby decreasing the trap elongation and avoiding the 1D BEC regime in which the initial coherence length drops drastically [32]. Based on *in-situ* imaging, the BEC length covers 6 lattice sites.

We hold the atoms in this trap for periods up to 500 ms and then release them. The release includes two steps: in the first 2.3 ms we “launch” the atoms away from the surface by suddenly increasing the current in the snake wire from 5.5 mA to 18 mA. During this step the cloud experiences a parabolic longitudinal confinement potential that creates a focussing effect after full release. Next, all potentials are turned off and the cloud experiences another 12 ms of free-fall under gravity (time-of-flight), following which an absorption image is taken.

Focusing plays a crucial role in the experiment. Under normal free-fall circumstances, corresponding to complete trap release in a single step, the diffraction pattern would develop its far-field appearance only after an impractical

long time-of-flight. Details of the focusing effect appear in [30].

An average of 30 consecutive images is presented in Fig. 2 (100 ms trap holding time). The zero-order and the first-order diffraction peaks are clearly visible. We have confirmed that the observed diffraction pattern periodicity of about 15 μm is independent of the trap-to-surface distance, the purity of the BEC, the position of the trapped cloud along the lattice, and the amplitude of the diffraction orders.

The observed contrast is typical of the superfluid (coherent) phase [33] and is much higher than would be expected from 30 images with random fringes, thus proving coherence (see also Fig. 3b), and more specifically determining that the coherence length spans at least several lattice sites. Beyond the known fact that heating and spin-flip rates for neutral atoms are small even so close to a room temperature surface, the rather surprising result of this experiment is that their most fragile feature, spatial coherence, is also maintained.

In Fig. 3a we examine a much larger sample (more than 1000 pictures) and for much longer holding times (up to 500 ms). Some contrast is lost relative to Fig. 2b

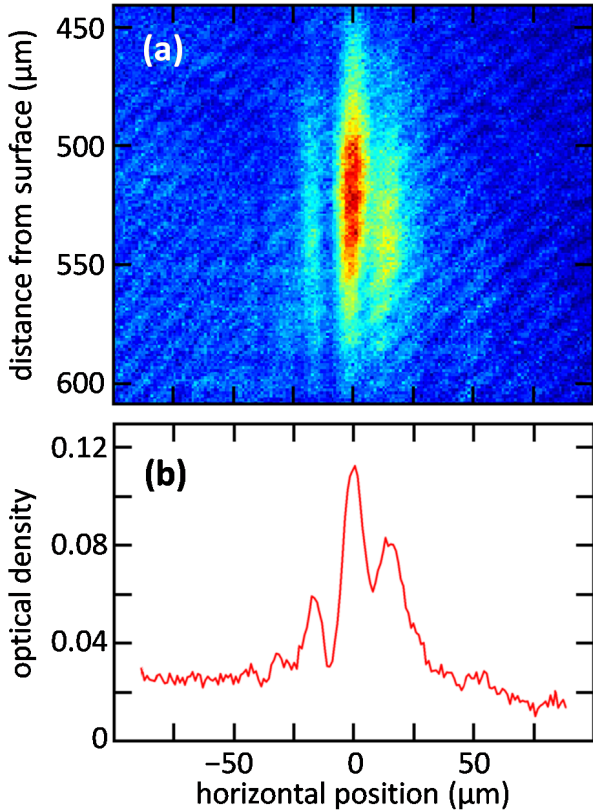


Fig. 2. (Color online) Experimental signal. Diffraction pattern observed after a trap holding time of $t = 100$ ms for 30 consecutive experimental cycles (no post-selection or post-correction is used). (a) Average of images acquired by absorption imaging. (b) A cut through the center of (a) showing the optical density (OD). The high contrast is highly unlikely to result from any random processes, thus demonstrating coherence (see text). Several possible explanations for the asymmetry observed in the amplitude of the first-order diffraction peaks are considered in [30].

due to the much larger number of experimental cycles used (spanning several days for each holding time), together with slight drifts of the lattice and experimental conditions during these measurements. The data in Fig. 3, unlike those in Fig. 2, are therefore post-selected for a range of atom-surface distances and horizontal placements of the trapped cloud.

The overall OD in Fig. 3a is seen to decrease with longer holding times, indicating an atom loss rate of 2.5 Hz, consistent with the measured spin-flip rate [30].

A BEC is expected to exhibit interference even when only short-range spatial coherence exists (*e.g.*, as in the free evolution of a 1D BEC). To show that our observed signals cannot arise from such short-range coherence, we compare our experimental results to simulated images expected from a random phase distribution amongst the magnetic lattice sites [30]. In the case of a random phase, the position of the diffraction peaks is different for each simulated image and an average over many images smears out the separate peaks and results in low contrast. For simplicity and robustness, we compare the OD difference

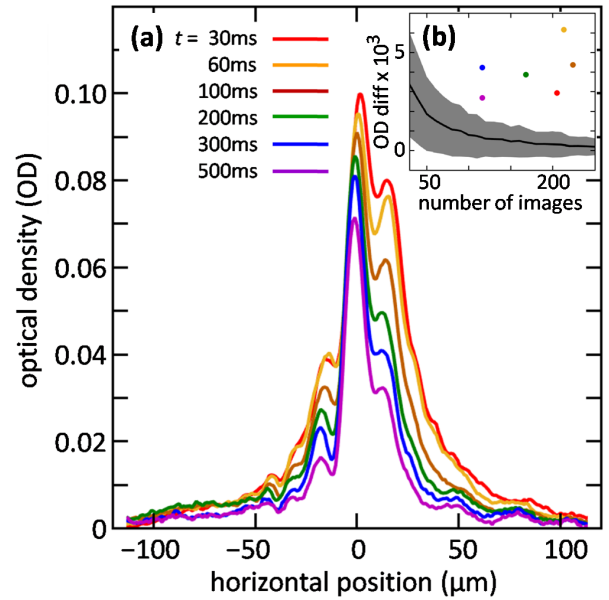


Fig. 3. (Color online) Robust spatial coherence. (a) Repeating the cut of Fig. 2b for trap holding times of $t = 30 - 500$ ms, averaged over all post-selected experimental cycles for each holding time (see [30] for our post-selection and post-correction procedures). Here we include a wide band along the vertical axis of Fig. 2a. We find that the first-order peaks are “locked” at about ± 15 μm , independent of t , for the > 1000 images collected in this figure. (b) Data points [same color code as in (a)] show the OD difference (“OD diff”) between the diffraction side-peak maxima and minima, averaged over all the experimental images obtained for each holding time. The black curve simulates how the same OD difference, after averaging a given number of images, drops towards zero for a random distribution of phases amongst the modulated potential wells. The shaded band around this curve shows one standard deviation for the average caused by these random phases. Lying far outside this band, the experimental OD difference data, as a direct experimental measure of the fringe visibility, show that the spatial coherence signal is robust even under varying experimental conditions.

of the diffraction side-peaks, defined as $\text{OD}_{\text{max}} - \text{OD}_{\text{min}}$ and obtained directly from the experimental fringe patterns as detailed in [30]. Fig. 3b shows this measure of fringe visibility as a function of the number of images averaged.

It is apparent that the experimental OD difference data is 2-10 standard deviations above the simulated random process, even for trap holding times up to 500 ms, and even when averaged over varying experimental conditions. While these numbers are excellent indicators, they are qualitative as systematic errors are not considered (since they would be very difficult to estimate accurately). A similar comparison for the data of Fig. 2b returns an even higher number of standard deviations.

Having thus shown spatial coherence even for a large number of cycles under varying experimental conditions, we now examine the rate of its dephasing. In Fig. 4, we show the contrast $[(\text{OD}_{\text{max}} - \text{OD}_{\text{min}})/(\text{OD}_{\text{max}} + \text{OD}_{\text{min}})]$, calculated as detailed in [30] as a function of holding

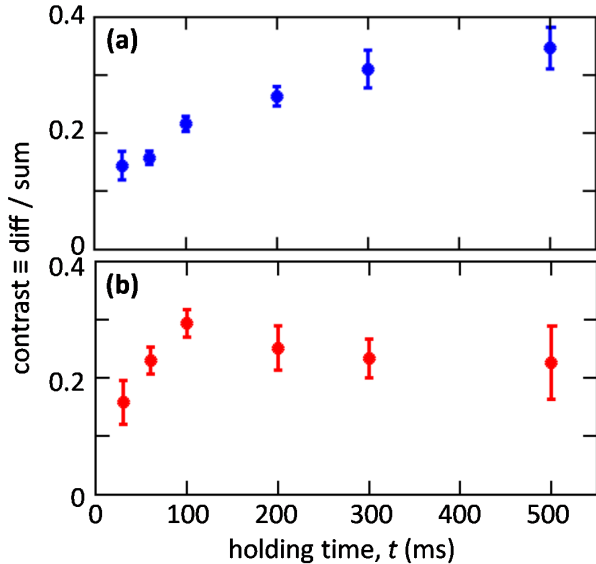


Fig. 4. (Color online) Spatial coherence dephasing rate. (a) Average contrast of the two first-order peaks for the data of Fig. 3a, using the standard definition of contrast, namely $(OD_{\max} - OD_{\min})/(OD_{\max} + OD_{\min})$. Error bars are extracted from a bootstrapping procedure [34]. (b) Repeating the analysis of (a) but selecting only images for each holding time t such that the number of atoms in the selected images all lie within the same range, independent of t . Error bars are calculated as in (a). The analysis in (b) removes effects caused by the reduction of the number of atoms with increasing holding time which could, for example, change the interatomic repulsion and distort some of the features of the diffraction patterns seen in Fig. 3a. The spatial coherence data is seen to be temporally robust as well, with little or no loss of contrast with time (*i.e.*, no dephasing).

time. This provides a direct estimate of the relative coherence for the different holding times, assuming that experimental imperfections that reduce the contrast are independent of the holding time. It is apparent from Fig. 3a that the rising contrast seen in Fig. 4a is related to the overall loss of atoms with increasing holding time. This atom loss evidently reduces the diffraction side-peaks at a proportionally faster rate than the central peak. In Fig. 4b we therefore re-plot the contrast data using a sub-group of 30-70 images for each holding time, selected so that all these images have an approximately equal number of atoms. This data sub-set is more immune to non-linear effects caused, *e.g.*, by atom-atom interactions.

The data are consistent with little or no dephasing. This is rather striking when one recalls that the BEC length is about $30\ \mu\text{m}$ and the correlation length of Johnson noise for an atom-surface distance of $5\ \mu\text{m}$ is also about $5\ \mu\text{m}$ [27]. In this regime, where spatial coherence is probed on a much larger scale than the distance to the surface, the dephasing rate is expected to be maximal [27]. This shows the robustness of spatial coherence near the surface, and opens the door for the future development of atomic circuits.

As an outlook, let us note that there is no precise determination of the dephasing rate due to Johnson noise Γ_D ([27] notes it should be “comparable” to the Johnson spin-flip rate), and consequently the very slow dephasing rate may be interpreted in two ways. First, if indeed the two rates are equal, then it may be that the estimated spin-flip rate of $1/6\ \text{Hz}$ [30] makes our experiment insensitive to the Johnson dephasing rate. However it may also be that Γ_D is larger than the Johnson spin-flip rate. In this case the theoretically likely value of $\Gamma_D/\Gamma_R < 1$, where Γ_R is the BEC rephasing rate [30], may mean that no dephasing can take place. (A large Γ_R is expected to be maintained for a very large dynamic range of tunneling and atom density [30]). In both cases the conclusion may be drawn that even for smaller heights and with different wire configurations, atomic circuits are feasible and should not be inhibited by lack of spatial coherence due to the nearby surface. Crossing the border to $\Gamma_D/\Gamma_R > 1$ by increasing the Johnson noise to technical noise ratio while moving to smaller heights will further improve our theoretical understanding. The effect of Johnson noise on BECs in guides is expected to be similarly weak and will enable atomic circuits with guides (*e.g.*, [35]), having the advantage of less phase diffusion due to atom-atom interactions.

Beyond the extensive Gross-Pitaevskii simulations we have conducted, further theoretical work is required in order to better explain the specific details of the observed diffraction pattern. As for atomic circuits, the next step should be to exhibit a high level of control over the tunneling rates. Advanced fabrication will contribute to improved results. For example, utilizing electrically anisotropic materials [36] is expected to reduce even further the Johnson noise responsible for dephasing. Utilizing crystalline materials such as carbon nano-tubes [37] or graphene sheets is expected to reduce both Johnson noise and potential corrugations due to electron scattering. Finally, to reduce the atom-surface distance by another order of magnitude, thus improving control over tunneling barriers, it would be beneficial to use nano-wires in order to considerably increase the gradients so that they can overcome the Casimir-Polder potential, as suggested for example in our earlier work [12]. Small wires can also enable geometries which will allow more flexibility in the choice of the magnetic field at the trap bottom and the frequency ratio (longitudinal to transverse) in the trap.

References

- [1] R. Folman, P. Krüger, J. Schmiedmayer, J. Denschlag, and C. Henkel. Microscopic atom optics: from wires to an atom chip. *Adv. At. Mol. Opt. Phys.* **48**, 263 (2002).
- [2] J. Reichel. Microchip traps and Bose-Einstein condensation. *Appl. Phys. B* **74**, 469 (2002).
- [3] J. Fortagh and C. Zimmermann. Magnetic microtraps for ultracold atoms. *Rev. Mod. Phys.* **79**, 235 (2007).
- [4] J. M. Obrecht, R. J. Wild, M. Antezza, L. P. Pitaevskii, S. Stringari, and E. A. Cornell. Measurement of the Tem-

perature Dependence of the Casimir-Polder Force. *Phys. Rev. Lett.* **98**, 063201 (2007).

[5] K. Maussang, G. E. Marti, T. Schneider, P. Treutlein, Y. Li, A. Sinatra, R. Long, J. Estève, and J. Reichel. Enhanced and reduced atom number fluctuations in a BEC splitter. *Phys. Rev. Lett.* **105**, 080403 (2010).

[6] M. F. Riedel, P. Böhi, Y. Li, T. W. Hänsch, A. Sinatra, and P. Treutlein. Atom-chip-based generation of entanglement for quantum metrology. *Nature* **464**, 1170 (2010).

[7] T. Langen, R. Geiger, M. Kuhmert, B. Rauer, and J. Schmiedmayer. Local emergence of thermal correlations in an isolated quantum many-body system. *Nature Physics* **9**, 640 (2013).

[8] T. van Zoest, N. Gaaloul, Y. Singh, H. Ahlers, W. Herr, S. T. Seidel, W. Ertmer, E. Rasel, M. Eckart, E. Kajari, S. Arnold, G. Nandi, W. P. Schleich, R. Walser, A. Vogel, K. Sengstock, K. Bongs, W. Lewoczko-Adamczyk, M. Schiemangk, T. Schuldt, A. Peters, T. Könemann, H. Müntinga, C. Lämmerzahl, H. Dittus, T. Steinmetz, T. W. Hänsch, and J. Reichel. Bose-Einstein Condensation in Microgravity. *Science* **328**, 1540 (2010).

[9] S. Machluf, Y. Japha, and R. Folman. Coherent Stern-Gerlach momentum splitting on an atom chip. *Nature Commun.* **4**, 2424 (2013).

[10] R. A. Pepino, J. Cooper, D. Z. Anderson, and M. J. Holland. Atomtronic Circuits of Diodes and Transistors. *Phys. Rev. Lett.* **103**, 140405 (2009).

[11] E. Charron, M. A. Cirone, A. Negretti, J. Schmiedmayer, and T. Calarco. Theoretical analysis of a realistic atom-chip quantum gate. *Phys. Rev. A* **74**, 012308 (2006).

[12] R. Salem, Y. Japha, J. Chabé, B. Hadad, M. Keil, K. A. Milton, and R. Folman. Nanowire atomchip traps for sub-micron atom-surface distances. *New J. Phys.* **12**, 023039 (2010).

[13] Y. J. Wang, D. Z. Anderson, V. M. Bright, E. A. Cornell, Q. Diot, T. Kishimoto, M. Prentiss, R. A. Saravanan, S. R. Segal, and S. Wu. Atom Michelson Interferometer on a Chip Using a Bose-Einstein Condensate. *Phys. Rev. Lett.* **94**, 090405 (2005).

[14] T. Schumm, S. Hofferberth, L. M. Andersson, S. Wildermuth, S. Groth, I. Bar-Joseph, J. Schmiedmayer, and P. Krüger. Matter-wave interferometry in a double well on an atom chip. *Nature Physics* **1**, 57 (2005).

[15] G.-B. Jo, Y. Shin, S. Will, T. A. Pasquini, M. Saba, W. Ketterle, D. E. Pritchard, M. Vengalattore, and M. Prentiss. Long Phase Coherence Time and Number Squeezing of Two Bose-Einstein Condensates on an Atom Chip. *Phys. Rev. Lett.* **98**, 030407 (2007).

[16] F. Baumgärtner, R. J. Sewell, S. Eriksson, I. Llorente-Garcia, J. Dingjan, J. P. Cotter, and E. A. Hinds. Measuring Energy Differences by BEC Interferometry on a Chip. *Phys. Rev. Lett.* **105**, 243003 (2010).

[17] Specifically, the splitting distance in these experiments, which determines the length over which spatial coherence is probed, was much smaller than the atom-surface distance and the correlation length of the noise. This is true even for experiments probing the entire coherence length of a BEC, which were not intended to measure the effect of external noise, but rather that of phase fluctuations due to atom-atom collisions [14]. Splitting the BEC over a distance much smaller than the correlation length of the external noise, they measured the relative phase between the two BECs over the length of the BEC, without direct interference or diffraction between remote parts of the BECs.

[18] Spatial coherence has also been probed by spatial splitting and then demonstrating spin coherence through the internal degrees of freedom [19].

[19] P. Böhi, M. F. Riedel, J. Hoffrogge, J. Reichel, T. W. Hänsch, and P. Treutlein. Coherent manipulation of Bose-Einstein condensates with state-dependent microwave potentials on an atom chip. *Nature Physics* **5**, 592 (2009).

[20] V. Y. F. Leung, D. R. M. Pijn, H. Schlatter, L. Torralbo-Campo, A. L. La Rooij, G. B. Mulder, J. Naber, M. L. Soudijn, A. Tauschinsky, C. Abarbanel, B. Hadad, E. Golan, R. Folman, and R. J. C. Spreeuw. Magnetic-film atom chip with $10\mu\text{m}$ period lattices of microtraps for quantum information science with Rydberg atoms. *Rev. Sci. Inst.* **85**, 053102 (2014).

[21] S. Jose, P. Surendran, Y. Wang, I. Herrera, L. Krzemien, S. Whitlock, R. McLean, A. Sidorov, and P. Hannaford. Periodic array of Bose-Einstein condensates in a magnetic lattice. *Phys. Rev. A* **89**, 051602(R) (2014).

[22] H. Bender, C. Stehle, C. Zimmermann, S. Slama, J. Fiedler, S. Scheel, S. Y. Buhmann, and V. N. Marachevsky. Probing Atom-Surface Interactions by Diffraction of Bose-Einstein Condensates. *Phys. Rev. X* **4**, 011029 (2014).

[23] D.-W. Wang, M. D. Lukin, and E. Demler. Disordered Bose-Einstein Condensates in Quasi-One-Dimensional Magnetic Microtraps. *Phys. Rev. Lett.* **92**, 076802 (2004).

[24] Y. Japha, O. Entin-Wohlman, T. David, R. Salem, S. Aigner, J. Schmiedmayer, and R. Folman. Model for organized current patterns in disordered conductors. *Phys. Rev. B* **77**, 201407(R) (2008).

[25] S. Aigner, L. Della Pietra, Y. Japha, O. Entin-Wohlman, T. David, R. Salem, R. Folman, and J. Schmiedmayer. Long-Range Order in Electronic Transport Through Disordered Metal Films. *Science* **319**, 1226 (2008).

[26] R. Stevenson, M. Hush, T. Bishop, I. Lesanovsky, and T. Fernholz. Sagnac interferometry with a single atomic clock. *arXiv:* 1504.05530v1 (2015).

[27] C. Henkel, P. Krüger, R. Folman, and J. Schmiedmayer. Fundamental limits for coherent manipulation on atom chips. *Appl. Phys. B* **76**, 173 (2003).

[28] C. Henkel and S. A. Gardiner. Decoherence of Bose-Einstein condensates in microtraps. *Phys. Rev. A* **69**, 043602 (2004).

[29] E. Boukobza, D. Cohen, and A. Vardi. Interaction-induced dynamical phase locking of Bose-Einstein condensates. *Phys. Rev. A* **80**, 053619 (2009).

[30] Details are provided in the Supplemental Materials section following the main text of this paper.

[31] S. Zhou, J. Chabé, R. Salem, T. David, D. Groswasser, M. Keil, Y. Japha, and R. Folman. Phase space tomography of cold-atom dynamics in a weakly corrugated potential. *Phys. Rev. A* **90**, 033620 (2014).

[32] S. Dettmer, D. Hellweg, P. Ryytty, J. J. Arlt, W. Ertmer, K. Sengstock, D. S. Petrov, G. V. Shlyapnikov, H. Kreutzmann, L. Santos, and M. Lewenstein. Observation of Phase Fluctuations in Elongated Bose-Einstein Condensates. *Phys. Rev. Lett.* **87**, 160406 (2001).

[33] M. Greiner, O. Mandel, T. Esslinger, T. W. Hänsch, and I. Bloch. Quantum phase transition from a superfluid to a Mott insulator in a gas of ultracold atoms. *Nature* **415**, 39 (2002).

[34] B. Efron and R. Tibshirani. Bootstrap Methods for Standard Errors, Confidence Intervals, and Other Measures of Statistical Accuracy. *Statist. Sci.* **1**, 54 (1986).

- [35] Y. Japha, O. Arzouan, Y. Avishai, and R. Folman. Using Time-Reversal Symmetry for Sensitive Incoherent Matter-Wave Sagnac Interferometry. *Phys. Rev. Lett.* **99**, 060402 (2007).
- [36] T. David, Y. Japha, V. Dikovsky, R. Salem, C. Henkel, and R. Folman. Magnetic interactions of cold atoms with anisotropic conductors. *Eur. Phys. J. D* **48**, 321 (2008).
- [37] P. G. Petrov, S. Machluf, S. Younis, R. Macaluso, T. David, B. Hadad, Y. Japha, M. Keil, E. Joselevich, and R. Folman. Trapping cold atoms using surface-grown carbon nanotubes. *Phys. Rev. A* **79**, 043403 (2009).

ACKNOWLEDGMENTS

We thank Julien Chabé, Ran Salem, and Tal David for the initial steps of the experiment, Zina Binstock for the electronics, and the BGU nano-fabrication facility for providing the high-quality chip. We are grateful to Amichay Vardi and Carsten Henkel for helpful discussions. This work is funded in part by the Israeli Science Foundation, the EC “MatterWave” consortium (FP7-ICT-601180), and the German-Israeli DIP project supported by the DFG. We also acknowledge support from the PBC program for outstanding postdoctoral researchers of the Israeli Council for Higher Education and from the Ministry of Immigrant Absorption (Israel).

SUPPLEMENTAL MATERIAL

We describe methods used to create and study the atomic cloud within a magnetic lattice, optimization of conditions necessary for this experiment, data analysis procedures, and procedures used for our simulation calculations.

MAGNETIC LATTICE, TRAP RELEASE, AND IMAGING

As in previous work [31], the experiment is conducted in an atom chip setup, shown schematically in Fig. 1a. The BEC is generated by collecting ^{87}Rb atoms in a magneto-optical trap and transferring them, in the $|F = 2, m_F = 2\rangle$ hyperfine state, into an elongated magnetic trap created by current in a copper Z-shaped trapping wire and bias fields in the x (longitudinal), y (imaging) and z (vertical) directions. After RF evaporative cooling, the BEC contains about 10^4 atoms and is about $340\text{ }\mu\text{m}$ from the atom chip surface.

Loading the magnetic lattice, whose potential modulation becomes effective $< 9\text{ }\mu\text{m}$ from the chip surface (Fig. 1c), is realized in two steps. The first step brings the condensate to about $25\text{ }\mu\text{m}$ from the atom chip surface by reducing the trapping-wire current while turning on the atom chip snake wire with a current of 30 mA . Simultaneously, we reduce the bias field in the x direction, thereby increasing the magnetic field at the trap minimum from 0.2 G to 18.3 G . At the end of the first step,

requiring 200 ms , the BEC is located in a trap potential produced by currents in both the trapping wire and the snake wire.

In the second step, we reduce the current in the snake wire to 5.5 mA , shifting the trap closer to the chip and turning the modulation on strongly (Fig. 1c). This second step is completed in 8 ms , a much shorter time than required for perfectly adiabatic loading; we carefully optimize a non-linear current ramp in order to avoid oscillation and excitation [38]. Fine adjustments of the trap position in the x , y and z directions are pre-determined by currents in a pair of U-shaped atom chip wires [31], the z -axis bias coils, and very slight changes in the trapping-wire current, respectively.

We do not measure the number of atoms in the magnetic lattice trap directly; such *in situ* measurements are only qualitative due to high magnetic fields and optical densities. After a brief holding time in the trap and subsequent release, we measure about 4000 atoms, indicating some loss on loading into the trap.

We use a high magnetic field of 18.3 G at the trap bottom mainly to achieve a lower trap aspect ratio, thereby avoiding the 1D BEC regime in which the spatial coherence length would drop drastically [32]. The lower transverse frequency also facilitates optimization of the “launching” stage implemented just before release. Smaller atom-surface distances could be achieved in future experiments by reducing the trap bottom in order to increase the potential barrier to the surface while maintaining the aspect ratio through more control over the longitudinal frequency.

The BEC is held for times $t = 30 - 500\text{ ms}$ in the magnetic lattice at a distance of about $5\text{ }\mu\text{m}$ from the atom chip surface. Trap frequencies in the longitudinal and transverse directions are $\omega_x = 2\pi \times 45\text{ Hz}$ (measured) and about $\omega_y \approx \omega_z = 2\pi \times 950\text{ Hz}$, respectively. The longitudinal frequency is measured for an atom-surface distance $> 9\text{ }\mu\text{m}$ where there is no potential modulation (Fig. 1c); calculations show that this frequency does not depend strongly on the distance from the surface. The transverse frequencies are calculated since they do depend strongly on the distance. Finally, we calculate a longitudinal frequency within each magnetic lattice site of about $\omega_{\text{site}} = 2\pi \times 500\text{ Hz}$ for an atom-surface distance of $5\text{ }\mu\text{m}$, about half of the transverse frequencies. *In-situ* absorption images show that the BEC is about $30\text{ }\mu\text{m}$ long, thereby filling 6 sites of the magnetic lattice.

We do not release the condensate immediately after the holding time t . Instead, we “launch” the condensate by suddenly (in $100\text{ }\mu\text{s}$) increasing the current in the snake wire from 5.5 mA to 18 mA . After a further 2.3 ms , we release the trap by turning off all currents and fields, finally allowing gravitational free-fall.

The launching process has two functions. First, it forces the atoms away from the chip so that they avoid crashing into the surface, which would otherwise occur as the atomic cloud expands. Second, and more important, the launching focuses the BEC, a critical feature for observing our diffraction patterns [39, 40].

We use resonant absorption imaging to measure the atomic density distribution after 12 ms of free-fall. Since the cloud is focused only in the x direction, its optical density drops quickly, thereby decreasing the signal-to-noise. Averaging over many images (*e.g.*, Fig. 2), which is done primarily to prove phase stability, therefore also suppresses noise from thermal background and other sources. Our half-width imaging resolution is about $7 \mu\text{m}$, which is insufficient to resolve the *in situ* atomic density modulation expected from the $5 \mu\text{m}$ -spacing between individual magnetic lattice sites. The imaging resolution is however, sufficient to resolve the atom cloud and its reflection produced by grazing incidence of the imaging laser beam on the reflective atom chip surface.

FOCUSING EFFECT

The mechanism of the focusing process is closely related to interatomic interactions within the BEC and therefore differs from atomic lensing for non-interacting atoms [41, 42]. Fig. 5 illustrates the focusing effect we observe for a BEC initially held $9 \mu\text{m}$ from the surface. At this distance, the $5 \mu\text{m}$ -period modulation potential has no influence (Fig. 1c), and the focusing effect may be understood by considering only the harmonic trapping potential. We measure a Thomas-Fermi full-width of $18 \mu\text{m}$, considerably narrower than a width of about $35 \mu\text{m}$ expected in the absence of focusing.

Here we briefly explain the effect of focusing and its importance for the observation of diffraction patterns emerging from a density- or phase-modulated BEC. We consider the evolution of the BEC after full release, whereupon we may assume that atom-atom interactions are negligible due to rapid expansion of the atomic cloud in the transverse directions. In this case, the free-space evolution of the initial wave function $\psi(\mathbf{r}, t_{\text{TOF}} = 0)$, in a reference frame moving with the freely falling center-of-mass, is given by

$$\psi(\mathbf{r}, t_{\text{TOF}}) = \int d^3\mathbf{k} \exp \left[i \left(\mathbf{k} \cdot \mathbf{r} - \frac{\hbar k^2 t_{\text{TOF}}}{2m} \right) \right] \tilde{\psi}(\mathbf{k}), \quad (1)$$

where

$$\tilde{\psi}(\mathbf{k}) = \frac{1}{(2\pi)^3} \int d^3\mathbf{r}' e^{-i\mathbf{k} \cdot \mathbf{r}'} \psi(\mathbf{r}', 0) \quad (2)$$

is the spatial Fourier transform of the initial wave function.

After a sufficiently long time, the expansion leads to a separation of the different momentum components; the far-field limit of the wave function is given by the stationary phase approximation, which yields

$$\psi(\mathbf{r}, t_{\text{TOF}}) \propto e^{imr^2/2\hbar t_{\text{TOF}}} \tilde{\psi}(\mathbf{k} = m\mathbf{r}/\hbar t_{\text{TOF}}), \quad (3)$$

such that the atomic density represents the Fourier transform of the initial wave function.

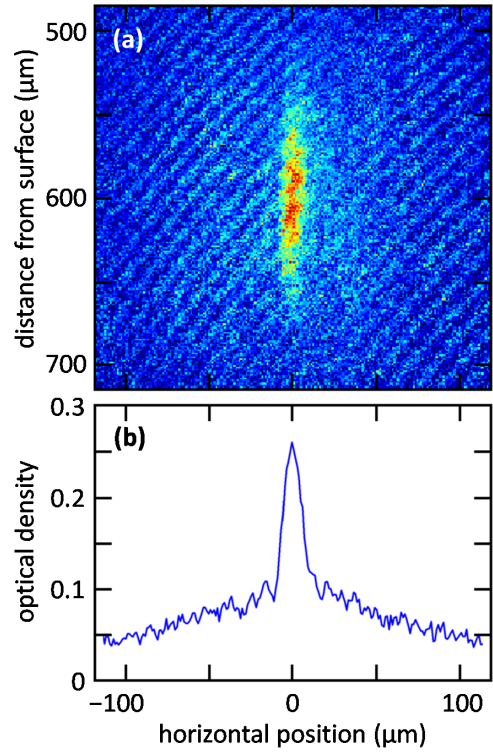


Fig. 5. (Color online) Focusing effect. (a) Single-shot image of a BEC, launched and released under the same conditions used throughout this work, and acquired after 12 ms of free-fall (time-of-flight). The BEC is initially held in a trap $9 \mu\text{m}$ from the surface, where there is no potential modulation, and no fringes are seen in the image. (b) A cut through the center of (a) with a measured Thomas-Fermi full-width of $18 \mu\text{m}$, compared to a width of about $35 \mu\text{m}$ calculated with no focusing. The thermal tails are seen to be unfocused.

More explicitly, by substituting Eq. (2) into (1) and integrating over the momentum \mathbf{k} , we obtain

$$\psi(\mathbf{r}, t_{\text{TOF}}) = \int d^3\mathbf{r}' G(\mathbf{r} - \mathbf{r}', t_{\text{TOF}}) \psi(\mathbf{r}', 0), \quad (4)$$

where

$$G(\mathbf{r} - \mathbf{r}', t) = \left(\frac{m}{2\pi i \hbar t} \right)^{3/2} \exp \left(i m \frac{|\mathbf{r} - \mathbf{r}'|^2}{2\hbar t} \right) \quad (5)$$

is the non-relativistic free-particle Feynman propagator. By expanding the square term in the exponent, we obtain

$$\psi(\mathbf{r}, t_{\text{TOF}}) = \left(\frac{m}{2\pi i \hbar t_{\text{TOF}}} \right)^{3/2} e^{imr^2/2\hbar t_{\text{TOF}}} \times \int d^3\mathbf{r}' \exp \left(-i \frac{m}{\hbar t_{\text{TOF}}} \mathbf{r} \cdot \mathbf{r}' \right) \exp \left(i \frac{mr'^2}{2\hbar t_{\text{TOF}}} \right) \psi(\mathbf{r}', 0). \quad (6)$$

The second exponent of the integral in Eq. (6) represents a quadratic phase which decreases with time as $1/t_{\text{TOF}}$. To attain the far-field form of a Fourier transform of the initial wave function as in Eq. (3) would therefore require a time $t_{\text{TOF}} \gg m\Delta x^2/2\hbar$, where Δx is the spatial extent of the initial atomic density along the x (longitudinal) direction. In our case, where $\Delta x \approx \pm 15 \mu\text{m}$, this

implies that a fully developed diffraction pattern would require $t_{\text{TOF}} > 150$ ms. This is much too long to allow observation in our system.

In order to overcome this limitation, we implemented a launching procedure, in which the atoms are kept in the harmonic potential for a time $\tau = 2.3$ ms even while being pushed away from the atom chip. Whereas before the launching procedure the atomic density along the x direction is determined by the equilibrium between the confining modulated harmonic potential and the repulsive force of the atom-atom interaction, after the beginning of launching the BEC expands in the radial direction and the repulsive force becomes considerably weaker. At this stage the harmonic force, no longer compensated by the strong repulsive potential, induces a velocity gradient along x , such that the atoms start to move towards the center. For a short time τ this velocity gradient is not sufficient to significantly change the atomic density and the main effect is to imprint a quadratic phase $\phi = -\alpha x^2$,

$$\psi(\mathbf{r}', 0) \rightarrow \psi(\mathbf{r}', 0) e^{-i\alpha x^2}, \quad (7)$$

where $\alpha = \frac{1}{2}m\omega_x^2\tau/\hbar$. When the atoms are finally released, this quadratic phase partially compensates for the quadratic phase in the second exponent of the integral in Eq. (6), such that after a finite time-of-flight $t_{\text{TOF}} = m/2\hbar\alpha \sim (\omega_x^2\tau)^{-1}$ the total quadratic phase in the integral vanishes completely, leading to a density pattern along the x direction that represents the Fourier transform of the initial density before launching, *i.e.*, a fully developed diffraction pattern as expected in the far-field limit.

The time-of-flight actually required for focusing is somewhat longer than the value of $(\omega_x^2\tau)^{-1}$ because repulsive forces do not completely vanish during the launching. Our Gross-Pitaevskii simulation (described below) predicts that the best focusing should occur at about $t_{\text{TOF}} = 8$ ms. We actually use a time-of-flight of $t_{\text{TOF}} = 12$ ms in order to allow further separation of the diffraction fringes; this additional delay does not significantly affect the sharpness of the diffraction peaks we observe, which is limited anyway by our finite optical resolution.

As shown in Fig. 5, the focusing does not affect thermal atoms in the atomic cloud, since this part of the atomic density is not dominated by the repulsive interactions, even when trapped during the holding time. These atoms continue to experience essentially the same harmonic potential during the launching as beforehand, so their state during the release is similar to their state before launching, and hence their expansion does not involve the focusing effect.

POST-SELECTION AND POST-CORRECTION

Averaging over multiple experimental cycles does not reduce the fringe contrast over short data accumulation periods (as shown in Fig. 2), but we must account for experimental drifts during longer runs that span many

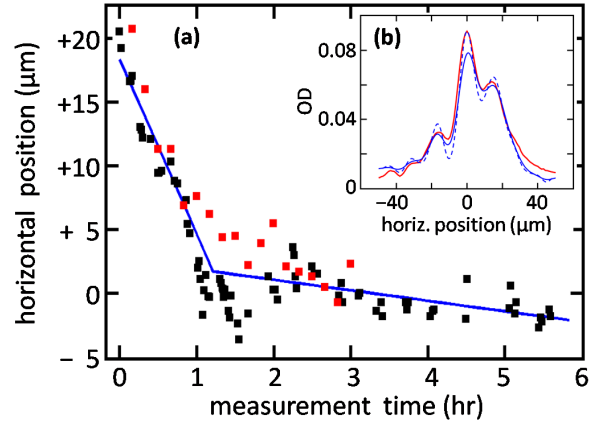


Fig. 6. (Color online) Experimental drifts and the effect of jitter. (a) Horizontal (x) position of the center of the atomic cloud, measured *in situ* during the first 3–5 hr of two experimental runs performed several weeks apart (black and red squares). The blue lines depict linear fits to a fast initial movement during the warm-up period, followed by a slower drift for the remainder of these experimental runs. (b) Loss of contrast that can be caused by residual “jitter” (*i.e.*, shot-to-shot variability in the *in situ* horizontal position) and inaccuracies in our post-correction procedures. The red curve is copied from the $t = 100$ ms data from Fig. 3a; the blue curves are calculated by applying random displacements along x to the high-contrast data of Fig. 2b, with standard deviations of $2.0\ \mu\text{m}$ (dashed) and $3.6\ \mu\text{m}$ (solid). It is apparent that residual jitter can cause some of the observed reduction in contrast between the data of Fig. 2b and Fig. 3a.

days. The atom chip mount is observed to move along the horizontal (x) direction during the course of our experimental measurements, and is apparent as motion of the *in situ* images, as shown in Fig. 6.

The initial warm-up period of the experiment produces a drift of about $20\ \mu\text{m}$ and appears to be caused by thermal stresses in the atom chip mount upon ohmic heating of the copper wires and their leads. The resulting translation of the entire atom chip mount equilibrates after about $1\text{--}1\frac{1}{2}$ hr of operation. We do not use data taken during this warm-up period. A much slower drift continues even after the warm-up period and appears to be caused by slight movements in the position of the trapping wire relative to the atom chip itself. As small as these slow-drift movements are however, they are a significant fraction of the magnetic lattice spacing and could cause significant smearing of the observed diffraction pattern.

The *in situ* x -axis position of the condensate depends on the harmonic potential created by the Z-shaped trapping wire. As discussed above, this harmonic potential also controls the BEC focusing, shifting the position of the diffraction pattern along the x axis in the same way as the shifts shown in Fig. 6. This provides a simple method to correct for these small slow-drift movements after the initial warm-up period.

For a given holding time, we acquire a series of 5–10 TOF images, after which we re-measure the *in situ*

position in an additional experimental cycle. Our post-selection procedure is then straightforward: we reject the entire series if the *in situ* horizontal position has wandered outside a range of $\pm 7 \mu\text{m}$ or if the actual distance from the atom chip is outside the range $z = 5.0 \pm 0.5 \mu\text{m}$. These selection criteria generally result in rejecting about 60-70% of the experimental cycles.

Our post-correction procedure then accounts for the slow drifts described above by shifting each measurement in the series by an average of the shifts observed in the *in situ* images taken at the beginning and end of the series. These corrections are always $\lesssim 3 \mu\text{m}$ since this is the maximum difference between successive *in situ* measurements, evident as the shot-to-shot variability during the slow-drift period in Fig. 6a. Finally, we average all the post-selected and post-corrected images for a given holding time. Despite various instabilities (*e.g.*, as depicted in Fig. 6b), these averages show stable fringes, even for experiments conducted over several weeks, accumulating over 1000 images (Fig. 3a).

We find an additional slow drift in the *in situ* distance of the cloud from the atom chip surface. This is due to vertical motion of the trapping wire due to ohmic heating of its copper leads, and results in a monotonically increasing atom-surface distance. We periodically adjust the trapping-wire current (by $< 2\%$) to maintain this distance within the range noted above and of course, we repeat the *in situ* calibration measurements before proceeding with further TOF acquisition.

ATOM-SURFACE DISTANCE

Our imaging resolution of about $7 \mu\text{m}$ affects the apparent distance of the cloud from the surface, as obtained from our *in situ* measurements. We use the measured *in situ* images for the post-selection procedures detailed above. Here we estimate systematic differences between the apparent distance obtained from the *in situ* images and the actual distance of the cloud from the surface.

In order to analyze the imaging procedure, we apply a low-pass filter for the spatial spectrum of the absorption pattern

$$\text{OD}(x, z) = -2 \log \left[\left| \mathcal{F}^{-1} \left\{ \mathcal{F} \left\{ e^{-n(x,z)\sigma_0/2} \right\} \times \theta(k_0^2 - k_x^2 - k_z^2) \right\} \right| \right], \quad (8)$$

where $\sigma_0 = 0.19 \mu\text{m}^2$ is the scattering cross-section of light with ^{87}Rb atoms, $n(x, z)$ is the column density of atoms, \mathcal{F} and \mathcal{F}^{-1} represent the Fourier and inverse Fourier transforms, and $\theta(k_0^2 - k^2)$ is the Heaviside function which allows only spectral components with wave vector smaller than k_0 to pass through the system due to the finite aperture of the imaging lens. We estimate that $k_0 \approx 2\pi/11.5 \mu\text{m}$. This procedure is equivalent to a convolution with an Airy function of about $7 \mu\text{m}$ radius representing the finite aperture of a lens (our diffraction-limited resolution is about $4 \mu\text{m}$ but this limit is not attained due to optical aberrations and shadowing of the lens by the atom chip).

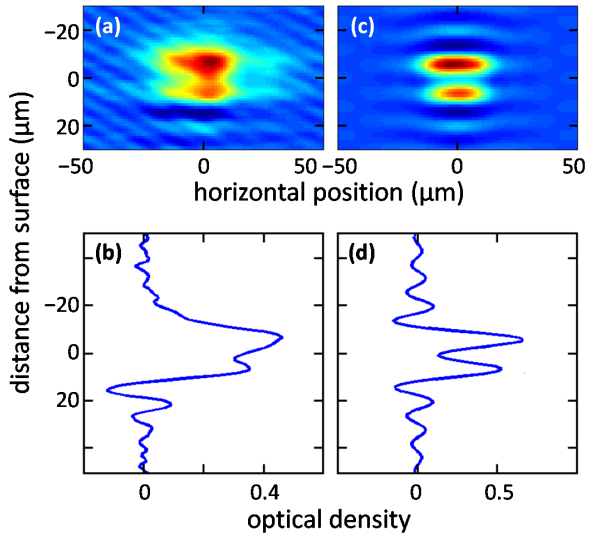


Fig. 7. (Color online) Atom-surface distance measurements: imaging the atomic cloud in the trap near the chip. (a) The experimental image shows the cloud and its reflection from the chip surface; a vertical cut through the center of the cloud is shown in (b) and yields a fitted atom-surface distance of $5.6 \mu\text{m}$. The image was smoothed with a Gaussian kernel 5 pixels wide in the horizontal (x) direction in order to reduce the experimental noise level. (c-d) The corresponding cloud and vertical cut for a Gross-Pitaevskii simulation (see text). The detection efficiency for the reflected cloud image is assumed to be reduced by 30% relative to the direct image. The simulation, whose peak positions match those of the experimental image, assumes an atom-surface distance of $4.8 \mu\text{m}$ and so we conclude that there is a systematic difference between the measured atom-surface distance and the actual distance of about $0.8 \mu\text{m}$.

In Fig. 7 we compare an experimental absorption image of the atomic cloud after holding in the modulated potential for 30 ms and a corresponding image of 4000 atoms having a density pattern obtained from our Gross-Pitaevskii simulations (see below). We set the center of the simulated cloud at $4.8 \mu\text{m}$ from the atom chip reflective surface. Since the atomic cloud and its reflection are separated by a distance comparable to the cutoff wavelength of the optical system, we see optical interference fringes in Fig. 7d that are also evident in the experimental image (b). Double-Gaussian fits yield a separation of $11.3 \mu\text{m}$ between the peak atom densities in both images. Since this translates to an apparent atom-surface distance of $5.6 \mu\text{m}$ for both the experimental and simulated cloud positions, we conclude that there is a systematic difference between the measured atom-surface distance and the actual distance, with the actual distance being about $0.8 \mu\text{m}$ less than the measured distance.

Similar effects due to optical resolution may also affect the spacing between our observed interference fringes, since they are also composed of a few peaks at distances comparable to the cutoff wavelength of the optical system. We discuss this further in connection to our detailed Gross-Pitaevskii simulations below.

CONTRAST ANALYSIS

The observed fringe patterns are asymmetric (details below) and their three peaks appear to have different widths, making it difficult to fit them with simple functional forms. We therefore applied the following automated algorithm to analyze each experimental image: (a) the central peak is identified; (b) secondary maxima are identified on the left side and the right side if they occur with a separation of 6-20 μm from the central peak; (c) if a secondary maximum cannot be found then the contrast on that side is defined to be zero; (d) if there are two or more maxima on one side then the highest one is chosen; (e) minima are identified between the side-peak maxima and the central peak.

In Fig. 3b we presented the OD difference as a direct experimental measure of fringe visibility. This OD difference is defined as the mean of $\text{OD}_{\text{max}} - \text{OD}_{\text{min}}$ obtained for the two sides, averaged over all the experimental images for a given holding time.

The contrast in Fig. 4 is calculated by defining an $\text{OD}_{\text{max}}^{\text{int}}$ value which is interpolated between the central and side peak at the position of the minimum on each side (*i.e.*, we define a triangular envelope on each side of the central peak). The (normalized) contrast is then defined as the mean of $(\text{OD}_{\text{max}}^{\text{int}} - \text{OD}_{\text{min}}) / (\text{OD}_{\text{max}}^{\text{int}} + \text{OD}_{\text{min}})$, again averaged over all the experimental images for a given holding time.

PHASE GRADIENTS AND RANDOMNESS; ASYMMETRY

We study the effect of phase randomization and phase gradients over the wave function in the modulated potential by using a simple numerical model. We start with a one-dimensional density function $\rho(x)$ composed of a Gaussian function centered at $x = 0$ and two side-band Gaussians at $x = \pm 15 \mu\text{m}$ whose maxima are half that of the main peak, as shown in Fig. 8a. This density distribution represents a diffraction pattern that is produced by a wave function with a periodically modulated amplitude and a constant phase over all the sites of the magnetic lattice. We introduce phase changes between the sites by first Fourier transforming the square root of the triple-Gaussian function $\sqrt{\rho}$ to obtain the periodically modulated function $\mathcal{F}\{\sqrt{\rho}\}$ and then introducing abrupt phase changes at the minima of this function, where the density is negligible. The phase is therefore constant within each site and varies only between sites. An inverse Fourier transform then re-generates the density function $\rho'(x)$ as modified by the phase changes imposed by our numerical model.

By introducing random phases between sites, we obtain noisy diffraction patterns like the one presented in Fig. 8b. Note that it becomes difficult to identify the zero-order and first-order peaks unambiguously and that smearing reduces the OD of the central peak by a factor of ≈ 2 even for individual patterns. Averaging a given number of similarly noisy patterns, each with its own ran-

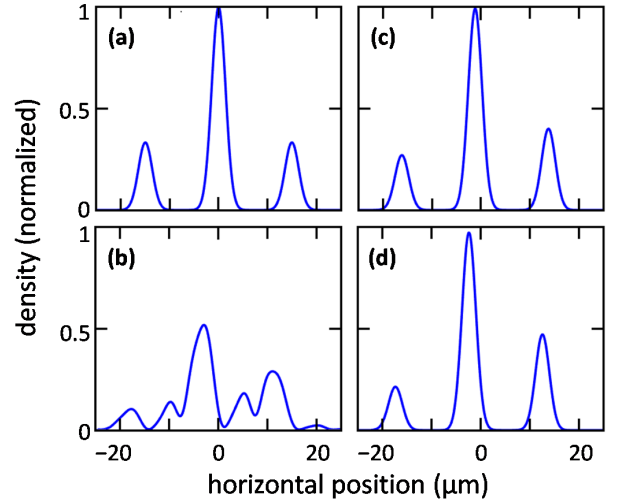


Fig. 8. (Color online) A simple model for the formation of an asymmetric diffraction pattern. (a) A symmetric diffraction pattern with two first-order peaks is formed by a Fourier transform of a wave function with a periodic amplitude and a constant phase. (b) A noisy diffraction pattern is obtained by applying a random phase between the sites. (c-d) Asymmetry between the two first-order peaks is obtained when a linear phase difference is applied between the sites (while keeping a constant phase within each site). Here (c) and (d) are obtained from a phase difference of 0.5 rad and 1 rad between adjacent sites, respectively (see text for possible sources of phase differences between sites). Note that, in addition to asymmetry, the fringe patterns in (c) and (d) also shift horizontally relative to (a).

dom phases between sites, is then used to generate the theoretical line and band shown in Fig. 3b. The line and band have been adjusted to correspond to a simulated central peak having an OD of about 0.1 in order to match the OD of the experimental peaks in Fig. 3a. The averaging rapidly reduces the expected OD difference as we increase the number of noisy patterns used.

By introducing a linear phase gradient instead, *i.e.*, equal phase jumps between the sites, we obtain an asymmetric diffraction pattern like those presented in Fig. 8c-d. This may explain some of the asymmetry observed in our experimental results. Other contributions to the observed asymmetry may include the slight rotation of the atomic cloud by the trapping wire (a well-known effect produced by currents in Z-shaped wires) and possible imperfections in the snake-wire fabrication [43].

SIMULATION OF ATOM DYNAMICS

In order to gain a quantitative understanding of the experimental results, we have performed extensive simulations of the dynamics of the atoms during the experiment, which takes into account the atom-atom interactions through the mean-field Gross-Pitaevskii (GP) theory. Here we describe the simulation procedure and present some of its results. The simulation is intended

to mimic the experimental conditions in a realistic manner, but it does not take into account possible systematic or random non-ideal effects such as imperfections of the system due to fabrication or mis-alignment of system elements or imperfections in the preparation of the BEC. Such imperfections may cause some of the asymmetry of the observed diffraction patterns, but a detailed explanation is beyond the scope of this paper.

The magnetic potential is calculated by applying the Biot-Savart law for the current density in the atom chip wires, as derived from a finite-element solution for the measured wire geometry. Unintended potential corrugations due to imperfections of the edge or bulk of the “snake” wire are not taken into account. The magnetic potential at a distance of a few μm from the snake wire has the approximate form

$$V(\mathbf{r}) \approx \frac{1}{2}m[\omega_x^2x^2 + \omega_y^2y^2 + \omega_z^2(z - z_0)^2] + V_0 e^{-(z-z_0)/l} \sin(kx), \quad (9)$$

where ω_x and $\omega_y \approx \omega_z$ are the (unmodulated) longitudinal and transverse frequencies respectively, $z_0 \approx 5 \mu\text{m}$ is the trapping distance, and $k = 2\pi/\lambda$ gives the periodicity of the potential modulation with $\lambda = 5 \mu\text{m}$. The amplitude of the modulation depends exponentially on the atom-surface distance with a range parameter of $l \approx 1 \mu\text{m}$; in addition, V_0 and the transverse frequencies depend parametrically on the trapping distance z_0 . Modulation of the longitudinal potential gives rise to a series of traps as shown in Fig. 1c, with each site having a frequency of $\omega_{\text{site}} \approx k\sqrt{V_0/m} \sim 2\pi \times 500 \text{ Hz}$, about half of the transverse frequencies ω_y and ω_z .

The simulation starts with N atoms in a BEC ground state that mimics the atomic cloud before it is loaded into the modulated potential. The modulation is then ramped up in 1 ms until the full potential is attained, at which time it may be approximated by Eq. 9 with $V_0 = 40 \text{ nK}$ (80 nK peak-to-valley). This ramp-up of the modulation provides an adequate approximation of the loading procedure, achieved experimentally by lowering the snake-wire current and thereby bringing the potential minimum to z_0 . After the potential modulation is turned on at time $t = 0$, the evolution in the trap is calculated up to 30 ms, corresponding to the shortest holding time used in our experiments. Snapshots of the atomic density in the trap for several times during this period are presented in Fig. 9a-e.

Given atom-surface distances of $5.0 \pm 0.5 \mu\text{m}$, consistent with our post-selection criteria, and a range of $N = 4000 \pm 1000$ atoms, we estimate that the chemical potential of the BEC is $\mu_{\text{calc}} \approx 125 \pm 30 \text{ nK}$. Noting that the modulation amplitude also depends on the atom-surface distance, we estimate that the chemical potential exceeds the barrier height by $\approx 45 \text{ nK}$. Dephasing effects are therefore expected to be suppressed by rephasing due to the overlap of atomic densities in the different sites. As noted in the following, a high rephasing rate is expected to continue even for a much smaller number of atoms, *i.e.*, even when the chemical potential is below the barrier height, since only a small tunneling rate is required.

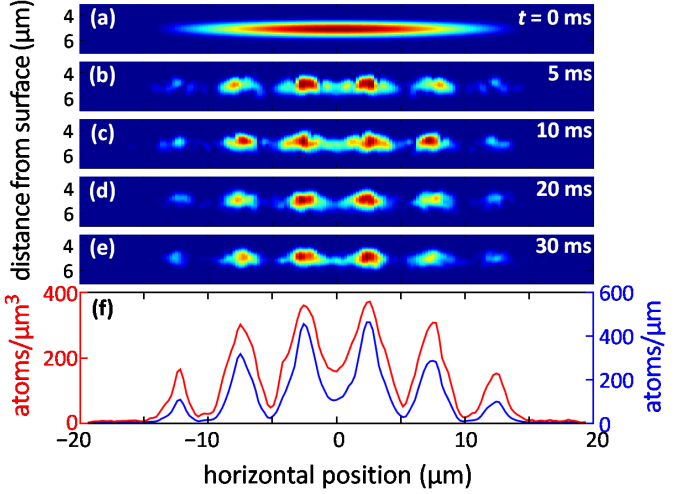


Fig. 9. (Color online) Simulation of evolution during holding time. (a) We simulate the loading of atoms into the modulated potential by starting from a ground state BEC of 4000 atoms in the nearly harmonic (unmodulated) potential. (b-e) The potential for an atom-surface distance of $5 \mu\text{m}$ is modulated by about 80 nK (peak to valley), resulting in a re-distribution of the atomic density, shown here for several holding times as atomic column densities in the x - z plane. (f) Atomic density per unit volume (red) and unit length (blue) are shown as an average over the holding times 5, 10, ..., 30 ms. In this simulation, the chemical potential exceeds the barrier height (see text). Rephasing of the BEC may therefore occur across the different magnetic lattices sites, despite random phase fluctuations applied by external noise. The density between the barriers becomes smaller with horizontal positions far from the center due to the rising longitudinal harmonic potential.

One should note that our GP simulation is based on a mean field theory and does not include possible effects of decoherence.

After the holding time we simulate launching of the BEC by ramping the current in the snake wire from 5.5 mA to 18 mA as described earlier. We solve the GP equation in a frame of reference that moves together with the center-of-mass of the atomic cloud. The shape and position of the atomic cloud during this launching process is shown in Fig. 10. After 2 ms the cloud arrives at the outer turning point of the potential and starts to accelerate back up towards the atom chip. Another 0.3 ms before the final trap release allows a longer period of time for the focusing and also increases the free-fall time before the cloud leaves the field-of-view of our imaging system. All currents and magnetic fields are then turned off and the cloud starts to fall freely in gravity.

After releasing the cloud, we calculate its free expansion for a time-of-flight of 12 ms. The simulated cloud develops a diffraction pattern with a central (zero-order) peak and several diffraction orders (Fig. 11), where each diffraction order is squeezed into a narrow wavepacket in the x -direction due to the focusing effect described above. Here we show only the column density of the atoms as

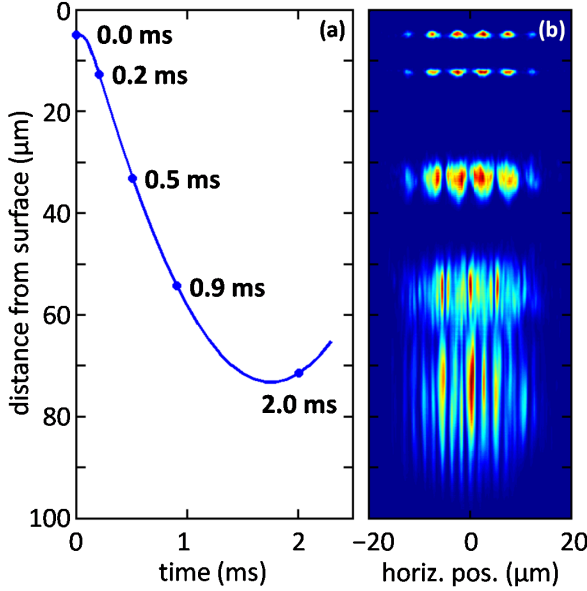


Fig. 10. (Color online) Simulated evolution of the atomic cloud during the launch. The cloud is ejected from the magnetic lattice by increasing the current in the snake wire from 5.5 mA to 18 mA in 100 μ s. (a) Trajectory of the center-of-mass of the cloud during the launch. The cloud arrives at the outer turning point (created by the trapping wire which is still on) and starts to accelerate back towards the atom chip before all currents are turned off (see text). Dots along the trajectory depict times at which the atomic density is shown in (b). (b) The diffraction pattern is seen to start forming already during the launch stage, while the atomic cloud starts to expand rapidly along the radial direction. Our optical resolution is currently unable to resolve detailed features of the expanding cloud during this period.

predicted by applying a low-pass filter to simulate the effect of our finite optical resolution.

ATOM LIFETIME

We investigate the expected dephasing due to the nearby surface by measuring the lifetime of atomic clouds held at varying atom-surface distances, as shown in Fig. 12. If we assume that these measured lifetimes are due entirely to Johnson and technical noise, then we can write

$$\tau_{\text{meas}}^{-1} = \tau_{\text{Johnson}}^{-1} + \tau_{\text{tech}}^{-1} = \frac{c_1}{d^2} + \frac{c_2}{d^2}, \quad (10)$$

where d is the atom-surface distance and c_1 and c_2 are coefficients for Johnson and technical noise, respectively [44, 45]. The expression for c_1 ignores cascading effects (*i.e.*, transitions amongst m_F Zeeman sub-levels that can re-populate the initial state) and geometrical factors (*e.g.*, assuming a layer of infinite extent). We will re-introduce these factors after the following preliminary analysis.

Fitting the experimental data of Fig. 12 yields $c_1 + c_2 = 65 \times 10^{-12} \text{ m}^2/\text{s}$, corresponding to the measured

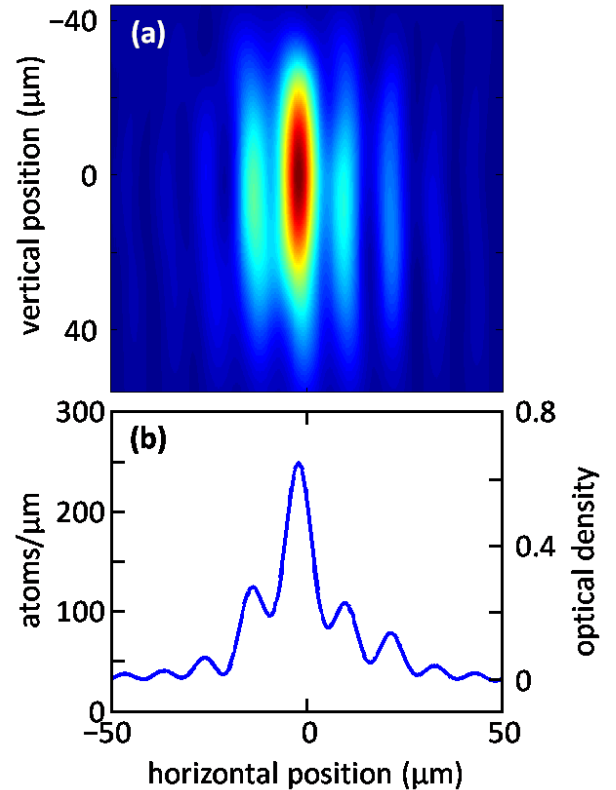


Fig. 11. (Color online) Simulated diffraction pattern after release. (a-b) The shape of the atomic cloud after 12 ms of free fall in the x - z plane, and a cut through the center of the cloud along the horizontal direction x , as they are expected to appear upon imaging with an optical system of finite resolution similar to ours. The observed asymmetry between the first-order peaks can arise from slight asymmetries in the magnetic potential near the snake wire due to the rotation of the cloud by the trapping wire (see text).

lifetime of 0.4 s at $d = 5 \mu\text{m}$. The coefficient c_1 can be estimated using the thin-film case of Eq. (4) in Ref. [44] and parameters that are appropriate for our experiment, yielding $c_1 = 8.5 \times 10^{-12} \text{ m}^2/\text{s}$ and in turn giving us $c_2 = 56 \times 10^{-12} \text{ m}^2/\text{s}$. These coefficients correspond to lifetimes for Johnson and technical noise of 3 s and 0.4 s at $d = 5 \mu\text{m}$.

Re-introducing cascading and geometrical effects [47] doubles the lifetime to 6 s for the Johnson noise component on our atom chip (dashed curve at $d = 5 \mu\text{m}$ in Fig. 12). Since Johnson noise has a very short correlation length, its spin-flip rate is expected to be “comparable” in value to the spatial coherence dephasing rate Γ_D [27]. Competing with Γ_D is the rephasing rate Γ_R , which may be estimated to be an order of magnitude slower than the Josephson frequency [29]. We cannot quote an estimated value for Γ_R due to significant uncertainties in the values of the chemical potential and the tunneling rate in our specific experiment. The correlation length of the technical noise dominating the spin-flip rate is similarly uncertain [48], prohibiting a reliable value for the Γ_D/Γ_R ratio. However, taking into account a chem-

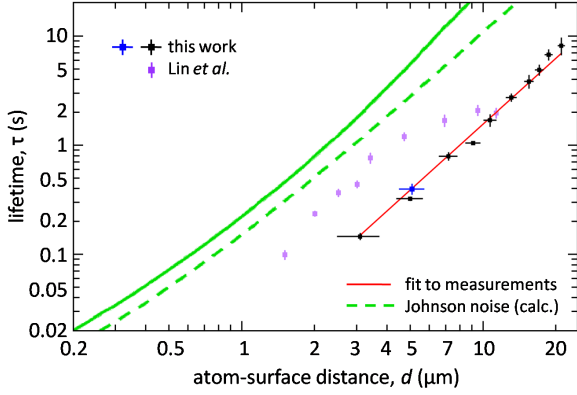


Fig. 12. (Color online) Atom chip noise: lifetimes measured for a range of atom-surface distances. The black data points are for thermal atoms with a magnetic field at the trap bottom of about 1 G while the blue datum is for a BEC under the same conditions as the experiments described throughout this paper. No appreciable difference is observed despite the higher trap bottom of 18.3 G used for the BEC. For comparison, we show data for conditions similar to those of our experiment and over a similar range of distances, but using no current in the surface closest to the atoms and therefore exhibiting much weaker technical noise [46]). The solid red line is the best-fit line for an assumed inverse quadratic dependence [Eq. (10)] using our measurements for thermal atoms. The green curves are calculated for spin flips due to Johnson noise only; the solid curve also accounts for cascading and geometric effects [47] while the dashed curve does not.

ical potential which is most probably above 100 nK and a similar potential modulation, tunneling is expected to be fast, and a ratio above one is unlikely.

References

- [38] J.-F. Schaff, X.-L. Song, P. Capuzzi, P. Vignolo, and G. Labeyrie. Shortcut to adiabaticity for an interacting Bose-Einstein condensate. *Europhys. Lett.* **93**, 23001 (2001).
- [39] Y. Castin and R. Dum. Bose-Einstein Condensates in Time Dependent Traps. *Phys. Rev. Lett.* **77**, 5315 (1996).
- [40] H. Ott, J. Fortágh, S. Kraft, A. Günther, D. Komma, and C. Zimmermann. Nonlinear Dynamics of a Bose-Einstein Condensate in a Magnetic Waveguide. *Phys. Rev. Lett.* **91**, 040402 (2003).
- [41] D. A. Smith, A. S. Arnold, M. J. Pritchard, and I. G. Hughes. Experimental single-impulse magnetic focusing of launched cold atoms. *J. Phys. B* **41**, 125302 (2008).
- [42] S. Zhou, Z. Duan, J. Qian, Z. Xu, W. Zhang, and Y. Wang. Cold atomic clouds and Bose-Einstein condensates passing through a Gaussian beam. *Phys. Rev. A* **80**, 033411 (2009).
- [43] R. C. Preston. Asymmetry in the diffraction pattern of a grating due to periodic errors. *Optica Acta: Int. J. Opt.* **17**, 857 (1970).
- [44] S. Scheel, P. K. Rekdal, P. L. Knight, and E. A. Hinds. Atomic spin decoherence near conducting and superconducting films. *Phys. Rev. A* **72**, 042901 (2005).
- [45] A. Emmert, A. Lupaşcu, G. Nogues, M. Brune, J.-M. Raimond, and S. Haroche. Measurement of the trapping lifetime close to a cold metallic surface on a cryogenic atom-chip. *Eur. Phys. J. D* **51**, 173 (2009).
- [46] Y. Lin, I. Teper, C. Chin, and V. Vuletić. Impact of the Casimir-Polder Potential and Johnson Noise on Bose-Einstein Condensate Stability Near Surfaces. *Phys. Rev. Lett.* **92**, 050404 (2004).
- [47] V. Dikovsky, Y. Japha, C. Henkel, and R. Folman. Reduction of magnetic noise in atom chips by material optimization. *Eur. Phys. J. D* **35**, 87 (2005).
- [48] We note that although technical noise should have no effect on the spatial coherence length because of its typically large correlation length, it may nevertheless introduce secondary effects through heating and spin-flips, and shot noise can include short correlation-length noise components.